



# Facile microwave-assisted green synthesis of Ag-ZnFe<sub>2</sub>O<sub>4</sub>@rGO nanocomposites for efficient removal of organic dyes under UV- and visible-light irradiation

Amr Hussein Mady <sup>a,b</sup>, Marjorie Lara Baynosa <sup>a</sup>, Dirk Tuma <sup>c</sup>, Jae-Jin Shim <sup>a,\*</sup>

<sup>a</sup> School of Chemical Engineering, Yeungnam University, Gyeongsan, Gyeongbuk 38541, Republic of Korea

<sup>b</sup> Petrochemical Department, Egyptian Petroleum Research Institute, Nasr City, Cairo 11727, Egypt

<sup>c</sup> BAM Federal Institute for Materials Research and Testing, Richard-Willstätter-Str. 11, 12489 Berlin, Germany

## ARTICLE INFO

### Article history:

Received 3 August 2016

Received in revised form

29 September 2016

Accepted 12 October 2016

Available online 14 October 2016

### Keywords:

ZnFe<sub>2</sub>O<sub>4</sub>

Graphene

Silver nanoparticle

Microwave synthesis

Photocatalysis

## ABSTRACT

Nanocomposites of Ag-ZnFe<sub>2</sub>O<sub>4</sub>@reduced graphene oxide (rGO) were synthesized using a one-pot microwave-assisted self-assembly method. The morphology and structure of the Ag-ZnFe<sub>2</sub>O<sub>4</sub>@rGO nanocomposites were characterized. The nanocomposites formed with 15.2 wt% rGO showed excellent adsorption properties and high photocatalytic activity for the degradation of methylene blue (MB), rhodamine B (RhB), and methyl orange (MO). The synergistic interactions between Ag, ZnFe<sub>2</sub>O<sub>4</sub>, and rGO decreased the aggregation of the nanoparticles (NPs) and increased the surface area, resulting in better absorption in both UV and visible light. Such a structure was helpful for separating the photo-excited electron-hole pairs and accelerating electron transfer. Electrochemical impedance spectroscopy (EIS) revealed a smaller resistance in the solid-state interface layer and charge transfer on the composite surface than that of the bare ZnFe<sub>2</sub>O<sub>4</sub> NPs and ZnFe<sub>2</sub>O<sub>4</sub>@rGO nanocomposite. The Ag-ZnFe<sub>2</sub>O<sub>4</sub>@rGO nanocomposite could be recovered easily by a magnet and reused five times with no significant decrease in photocatalytic activity. The as-prepared Ag-ZnFe<sub>2</sub>O<sub>4</sub>@rGO nanocomposite catalyst could be applied to the removal of hard-to-degrade waste materials owing to its high efficiency in both UV and visible light and its excellent reusability.

© 2016 Elsevier B.V. All rights reserved.

## 1. Introduction

Organic dye effluents from the textile and dyeing industries and other industrial processes utilizing dyes are one of the largest groups of pollutants discharged into the local environment at the respective production sites without adequate treatment [1,2]. Although conventional biological, physical, and chemical methods have been established for wastewater treatment, in these cases, the pollutant is only transferred from the liquid phase to the solid phase and further treatment is necessary to purify the resulting sludge. Additionally, pollutants with very low concentrations are still difficult to remove from wastewater [3]. Advanced oxidation processes (AOPs) have been used to remove a wide range of organic contaminants from water and air [4]. In this context, heterogeneous photocatalysis is considered one of the most potent AOPs

because of its potential applications in the degradation of organic contaminants [5].

So far, semiconductors, such as TiO<sub>2</sub>, ZnO, and SnO<sub>2</sub>, have been studied extensively as semiconductor photocatalysts. The wide band gap (3.0–3.8 eV) of these semiconductors limits their photocatalytic activity under visible-light irradiation [6–8]. Many spinel-type oxides show photocatalytic activity in the visible-light range [9–12]. Among these materials, the spinel ZnFe<sub>2</sub>O<sub>4</sub> is a potential candidate for visible-light photocatalysis due to its narrow band gap (1.9 eV), low toxicity, natural abundance, excellent ferromagnetic properties for magnetic separation from suspensions, and overall environmental benignity [13,14]. Most recently in 2016, Cai et al. prepared ZnFe<sub>2</sub>O<sub>4</sub> using a two-step method and evaluated its photocatalytic activity for the degradation of Orange II dye under visible-light irradiation through the splitting of H<sub>2</sub>O<sub>2</sub> to generate highly reactive •OH radicals [15]. On the other hand, Orange II cannot be degraded by bare ZnFe<sub>2</sub>O<sub>4</sub> due to the rapid recombination of photogenerated electron-hole pairs from a low valence-band potential and an accompanying poor photoelectric effect [16].

\* Corresponding author.

E-mail address: [jjshim@yu.ac.kr](mailto:jjshim@yu.ac.kr) (J.-J. Shim).

To address the above-mentioned problems and to achieve good performance, several researchers have developed novel routes. Graphene has fascinating properties, such as a large surface area, good mechanical flexibility, high chemical stability, and unique electronic properties [17]. Graphene is considered an ideal substrate to form graphene-based nanocomposites by anchoring nanoparticles on the layer surface, which make the resulting nanocomposite an efficient photocatalyst, because of the enhanced adsorption on the catalyst, non-aggregation of nanoparticles, an extended light-absorption range, and a significantly less recombination of photogenerated electron-hole pairs [14]. In addition, silver nanoparticles show strong visible-light absorption due to their surface plasmon resonance (SPR) [18]. This enhances the photocatalytic activity of the nanocomposite, and Ag NPs work as an electron sink, facilitating charge separation of the photogenerated electron-hole pair [17]. A range of metal ferrite-graphene nanocomposites have been reported [19–21]. Yao et al. synthesized magnetic ZnFe<sub>2</sub>O<sub>4</sub>-graphene nanocomposites [22]. The photocatalytic activity of Orange II under visible light in the presence of peroxyomonosulfate (PMS) was evaluated in their work. Fu and Wang synthesized ZnFe<sub>2</sub>O<sub>4</sub>-graphene for the removal of methylene blue in the presence of H<sub>2</sub>O<sub>2</sub> under visible-light irradiation [23]. Zhu et al. prepared Ag/MFe<sub>2</sub>O<sub>4</sub> (M=Zn, Cu, Co, and Ni) catalysts using a traditional wet impregnation technique and tested these for the photodegradation of 4-chlorophenol under visible-light irradiation [24]. Khadgi et al. synthesized a ZnFe<sub>2</sub>O<sub>4</sub>-Ag/reduced graphene oxide (rGO) nanocomposite via a sophisticated solvothermal reaction and evaluated the performance of the nanocomposite by the degradation of 17 $\alpha$ -ethinylestradiol (EE2) under visible-light irradiation in the presence of humic acid [25]. The presence of the Ag NPs accelerated the rate of degradation of the organic compounds due to the enhanced separation of photogenerated electron-hole pairs in the ultraviolet and visible region.

The microwave-assisted synthesis is considered an attractive method for the preparation of materials. Microwaves excite the dipoles of the molecules to intensify their rotations and vibrations and generate heat that is homogeneous and quickly dispersed within the entire reactor due to the increased friction between molecules. Therefore, the mechanisms of a microwave method are more closely related to the molecular structures and properties than those of the conventional heating. Highly mono-dispersed oxide nanoparticles, such as ZnFe<sub>2</sub>O<sub>4</sub>-graphene nanocomposite [7], rGO/Ag<sub>3</sub>PO<sub>4</sub> [26], and graphene-TiO<sub>2</sub> hybrid [27], have been prepared via a microwave method. Under microwave irradiation, the volume of GO expanded and, from the pyrolytic process, a large amount of gas emission was observed. After the pyrolysis reaction, GO with a high oxygen content was transformed to pyrolyzed (reduced) graphene oxide, which then underwent a deoxygenization reaction under microwave irradiation [28]. Microwave heating is more efficient in terms of the energy used, requires less time for synthesis, and produces higher temperature homogeneity; particle sizes in the range of 15–35 nm have been obtained.

In this study, magnetically separable Ag-ZnFe<sub>2</sub>O<sub>4</sub>@rGO nanocomposites with varying graphene contents were synthesized by a simple one-pot hydrothermal method using microwaves at a low temperature and a very short time without a surfactant or template. The reduction of graphene oxide (GO) to rGO and the in-situ deposition of ZnFe<sub>2</sub>O<sub>4</sub> NPs and Ag NPs on rGO occurred simultaneously in a one-pot reaction. The synthesized Ag-ZnFe<sub>2</sub>O<sub>4</sub>@rGO nanocomposites exhibited high photocatalytic activity on the degradation of the dyestuffs methylene blue (MB, C.I. 52015), rhodamine B (RhB, C.I. 45170), and methyl orange (MO, C.I. 13025) under both UV- and visible-light irradiation. Moreover, the magnetic properties of ZnFe<sub>2</sub>O<sub>4</sub> make the separation of the nanocomposite easier, avoiding environmental contamination

from processing. Similarly, the nanocomposites showed high photocatalytic stability and reusability. A possible mechanism for the degradation of dyes under the administration of Ag-ZnFe<sub>2</sub>O<sub>4</sub>@rGO and UV- or visible-light irradiation is also explained in detail.

## 2. Experimental

### 2.1. Materials and sample synthesis

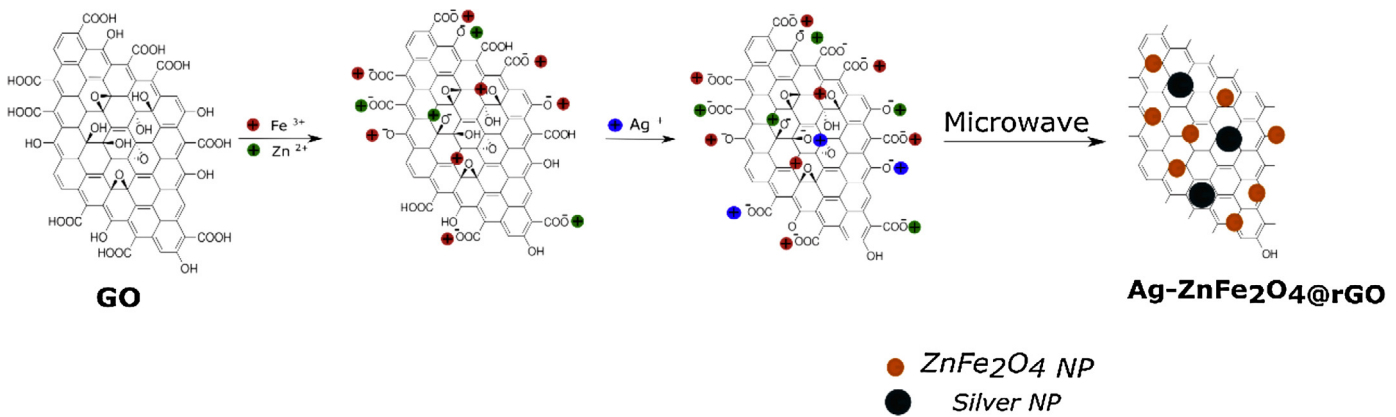
All reagents employed in the present study that were purchased from Alfa Aesar were of analytical grade and used without further purification. Graphene oxide (GO) was generated by the oxidation of graphite powder under acidic conditions according to Tour's method [29].

The Ag-ZnFe<sub>2</sub>O<sub>4</sub>@rGO nanocomposites were synthesized by a low-temperature, microwave-assisted, self-assembly precipitation method. Scheme 1 presents the proposed formation mechanism of the Ag-ZnFe<sub>2</sub>O<sub>4</sub>@rGO nanocomposites. Typically, 2 mmol of FeCl<sub>3</sub>·6H<sub>2</sub>O and 1 mmol of Zn(CH<sub>3</sub>COOH)<sub>2</sub>·2H<sub>2</sub>O were dissolved in 10 ml of deionized water, and 80 mg of GO was dispersed in 60 ml of deionized water and treated ultrasonically for 1 h. The solution containing Fe<sup>3+</sup> and Zn<sup>2+</sup> was added to the GO dispersion followed by stirring for 30 min. Subsequently, 10 ml of 0.1 M AgNO<sub>3</sub> was added to the resulting mixture followed by stirring for 30 min. Ultimately, a 4 ml portion of 5 M N<sub>2</sub>H<sub>4</sub>·H<sub>2</sub>O was added with stirring for another 30 min. The resulting suspension was transferred to a 2.45 GHz microwave reactor (CEM Discover), heated to 100 °C (150 W) under atmospheric pressure and maintained at that temperature for 10 min before being cooled to room temperature. Finally, the samples were collected by centrifugation, washed repeatedly with deionized water and absolute ethanol, and dried in a vacuum oven at 60 °C for 2 h. For comparison, bare ZnFe<sub>2</sub>O<sub>4</sub> (Fig. S1) and ZnFe<sub>2</sub>O<sub>4</sub>@rGO (Fig. S2) were also prepared using the same process described above for Ag-ZnFe<sub>2</sub>O<sub>4</sub>@rGO without the addition of AgNO<sub>3</sub> and GO, and AgNO<sub>3</sub>, respectively.

To determine the effects of the GO loading, Ag-ZnFe<sub>2</sub>O<sub>4</sub>@rGO nanocomposites with different amounts of GO (20, 40, 80, and 100 mg) were also prepared, and the corresponding products are denoted as Gx (where x=20, 40, 80, and 100 mg).

### 2.2. Characterization

Several different methods were applied to characterize the samples. X-ray powder diffraction (XRD; PANalytical, X'Pert-PRO MPD) was carried out using Cu K $\alpha$  radiation. The morphology and structure of the as-prepared materials were determined by field-emission scanning electron microscopy (FE-SEM; Hitachi S-4800). Transmission electron microscopy (TEM; Philips, CM 200) images were collected at an acceleration voltage of 200 kV. Fourier-transform infrared (FT-IR) spectroscopy of the samples was performed on a Bio-Rad Excalibur Series FTS 3000 spectrometer. Raman spectroscopy was carried out using a model XploRA plus (HORIBA) Raman spectrometer. An investigation of the surface components of the samples was carried out by X-ray photoelectron spectroscopy (XPS; AXIS Nova) using Al K $\alpha$  monochromatized radiation. The BET (Brunauer-Emmett-Teller) surface area ( $S_{\text{BET}}$ ) and the pore-size distribution of the samples were investigated using a N<sub>2</sub> adsorption-desorption apparatus Micromeritics 3Flex Surface Characterization Analyzer (Micromeritics Instruments) at a temperature of –196 °C. Prior to the adsorption-desorption experiments, the samples were degassed at 180 °C for 12 h. The BET specific surface areas were obtained by applying the BET equation, and the pore-size distribution was obtained using the Barrett-Joyner-Halenda (BJH) method. Thermogravimetric analysis (TGA) and differential scanning calorimetry (DSC) of the samples were



**Scheme 1.** Schematic illustration of the preparation of Ag-ZnFe<sub>2</sub>O<sub>4</sub>@rGO nanocomposites by a short microwave-assisted self-assembly method.

carried out on a TA Instruments SDT Q600 thermogravimetric analyzer at a heating rate of 10 K min<sup>-1</sup> in air and nitrogen atmosphere. The silver content of the composite was determined by inductively coupled plasma-atomic emission spectrometry (ICP-AES, PerkinElmer). The UV-vis diffuse reflectance spectra (DRS) of the samples were obtained using a Varian Cary 5000 UV-vis-NIR spectrophotometer.

### 2.3. Electrochemical impedance spectroscopy (EIS) study

EIS was performed using an Autolab PGSTAT302 N (Metrohm) instrument. The measurements were conducted in a conventional three-electrode cell system. The working electrode was prepared by depositing the active material (bare ZnFe<sub>2</sub>O<sub>4</sub>, ZnFe<sub>2</sub>O<sub>4</sub>@rGO, or Ag-ZnFe<sub>2</sub>O<sub>4</sub>@rGO) on fluorine-tin oxide (FTO) glass (1 cm<sup>2</sup> active area) by the drop-casting method. Here, the Ag/AgCl electrode, the Pt electrode, and 0.1 M KCl in 5 mM K<sub>3</sub>[Fe(CN)<sub>6</sub>] were employed as the reference electrode, the counter electrode, and the electrolyte, respectively. The measurements were performed in the dark at a potential window of 0 to 0.6 V at a scan rate of 25 mV s<sup>-1</sup>. The impedance spectra of the samples were recorded over the frequency range from 100 kHz to 0.01 Hz.

### 2.4. Photocurrent measurements

The photocurrent was measured on an Autolab PGSTAT302 N (Metrohm) instrument. The test electrodes were prepared according to Ref. [19]. The working electrode was prepared by depositing the active material (i.e., bare ZnFe<sub>2</sub>O<sub>4</sub> or Ag-ZnFe<sub>2</sub>O<sub>4</sub>@rGO) on a fluorine-tin oxide (FTO) glass (0.5 cm<sup>2</sup> active area) by the drop-casting method. A 10-W UV lamp ( $\lambda = 254$  nm) was used as the light source.

### 2.5. Photocatalytic activity measurement

The photocatalytic activity of the as-prepared samples was evaluated by the photocatalytic degradation of MB under both UV- and visible-light irradiation. The reactions were carried out in a photoreactor at a temperature of approximately 25 °C. Typically, 25 mg of the photocatalyst was dispersed in 50 ml of an aqueous MB solution (20 ppm) and then stirred in the dark for 30 min to achieve an adsorption-desorption equilibrium. A 40-W UV lamp (UV-light source,  $\lambda = 365$  nm) and a 400-W overhead projector lamp (OHP) (visible-light source,  $\lambda > 420$  nm) were used in the photoreaction. At predetermined time intervals, 3 ml of liquid was withdrawn from the reaction solution and separated through centrifugation (13000 rpm, 10 min). To examine the universality of the obtained samples as an example for the degradation of organic pollutants, in

this work especially on different types of dyes, the same set of procedures was carried out separately on 50 ml of aqueous solutions (10 ppm) of MB, RhB, and MO. The concentrations of MB, RhB, and MO in the solution were determined by UV-vis spectrophotometry at wavelengths of 663, 553, and 460 nm, respectively.

To investigate the photocatalytic stability and reusability of the samples, the photocatalytic activity measurements mentioned above were repeated for 5 cycles using an aqueous MB solution (20 ppm). After each cycle, the spent photocatalysts were separated from the treated MB solution, washed with deionized water, dried in an oven, and used again for the next photodegradation cycle [30].

The photocatalytic degradation followed pseudo-first-order kinetics, which is expressed as

$$\ln(C_0/C_t) = kt \quad (1)$$

where  $k$  is the apparent rate constant,  $C_0$  is the initial concentration of the pollutant after the adsorption-desorption equilibrium, and  $C_t$  is the residual concentration of pollutant in the solution collected at regular time intervals under both UV- and visible-light irradiations. To further examine the photocatalytic mechanism, trapping experiments were performed to determine the dominant reactive species involved in photodegradation of the MB dye. The trapping experiment was similar to the photocatalytic activity measurements except for the addition of scavenger compounds, i.e., 0.001 M *p*-benzoquinone (BZQ), 0.1 M isopropyl alcohol (IPA), or 0.1 M sodium bicarbonate (NaHCO<sub>3</sub>) [3].

## 3. Results and discussion

### 3.1. Phase structure and morphology

**Fig. 1** presents XRD patterns of the as-prepared bare ZnFe<sub>2</sub>O<sub>4</sub> NPs, ZnFe<sub>2</sub>O<sub>4</sub>@rGO and Ag-ZnFe<sub>2</sub>O<sub>4</sub>@rGO nanocomposites. For these XRD patterns, the peaks at 30.1, 35.3, 43.0, 53.5, 56.3, and 62.4° 2θ were indexed to the (220), (311), (400), (422), (511), and (440) crystal planes of spinel-type ZnFe<sub>2</sub>O<sub>4</sub> (JCPDS 22-1012), respectively. For the ZnFe<sub>2</sub>O<sub>4</sub>@rGO nanocomposite, an additional weak broad peak was observed at 18–22° 2θ, which can be indexed to reduced graphene oxide. Bare rGO exhibits its characteristic peak (002) at the 18–25° 2θ range, but the XRD peak for rGO was not detected in the Ag-ZnFe<sub>2</sub>O<sub>4</sub>@rGO nanocomposite. This can be attributed to the effective minimization of the restacking of rGO sheets after reduction by anchoring Ag and ZnFe<sub>2</sub>O<sub>4</sub> NPs as spacers. Moreover, additional XRD peaks at 38.12, 44.28, 64.43, and 77.47° 2θ were assigned to the (111), (200), (220), and (311) crystal planes of Ag (JCPDS 04-0783) in the Ag-ZnFe<sub>2</sub>O<sub>4</sub>@rGO nanocomposite.

**Fig. 2(a-c)** presents FE-SEM and TEM images of the synthesized Ag-ZnFe<sub>2</sub>O<sub>4</sub>@rGO nanocomposite. The ZnFe<sub>2</sub>O<sub>4</sub> and Ag NPs were

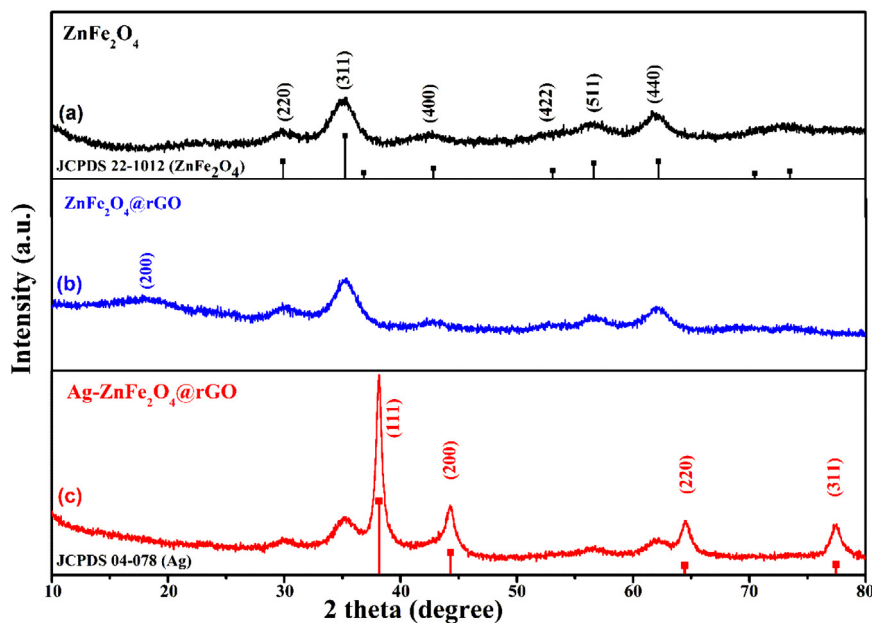


**Fig. 1.** XRD pattern of (a) bare  $\text{ZnFe}_2\text{O}_4$ , (b)  $\text{ZnFe}_2\text{O}_4$ @rGO, and (c) Ag- $\text{ZnFe}_2\text{O}_4$ @rGO (G80).

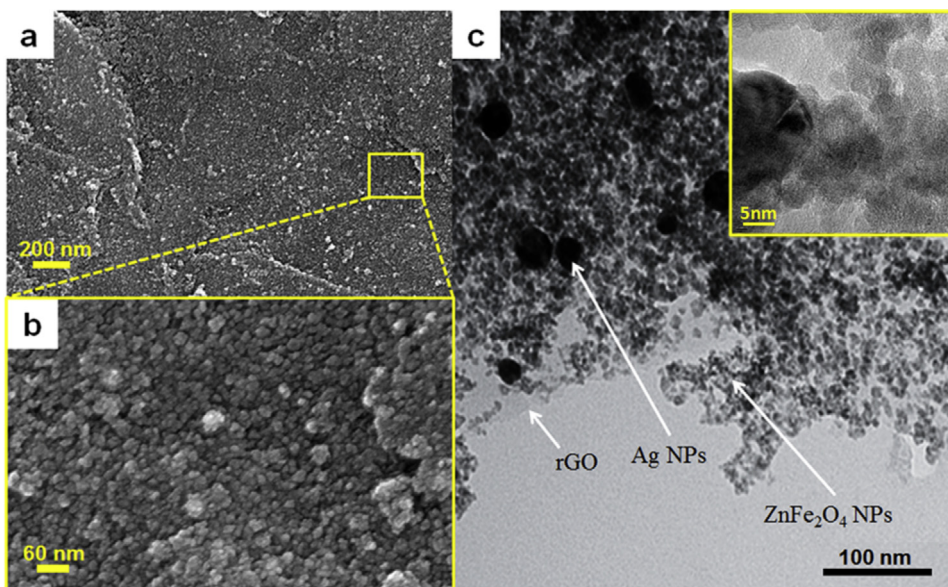


**Fig. 2.** FE-SEM images (a, b) and TEM images (c) of Ag- $\text{ZnFe}_2\text{O}_4$ @rGO (G80). The inset presents the high-resolution TEM image.

approximately 10–20 nm and 30–40 nm in size (cf. Fig. 2b and c), respectively. This suggests that the mutual interactions between the  $\text{ZnFe}_2\text{O}_4$  NPs and hierarchical flexible graphene sheets limit the agglomeration of the crystalline  $\text{ZnFe}_2\text{O}_4$  NPs (Fig. S1) to some extent. TEM (Fig. 2c) revealed the intimate hybrid structure of the photocatalyst, where  $\text{ZnFe}_2\text{O}_4$  NPs and silver NPs were deposited on the surface of the large rGO sheets. The high-resolution TEM (HRTEM) image of the composite (upper right inset in Fig. 2c) clearly shows a large silver particle (in black) and many adjacent smaller Ag- $\text{ZnFe}_2\text{O}_4$ @rGO particles (in gray). Both the edge of rGO and the nanostructure of  $\text{ZnFe}_2\text{O}_4$  NPs and silver NPs could be observed clearly in the TEM image of higher magnification. This strong mutual interaction among the  $\text{ZnFe}_2\text{O}_4$  NPs, silver NPs, and the graphene sheets enables rapid electron transport, thus guaranteeing efficient chemical performance.

The surface chemical composition and electronic state of the Ag- $\text{ZnFe}_2\text{O}_4$ @rGO nanocomposite can be seen on the XP spectra in Fig. 3. The survey spectra (Fig. 3a) revealed the presence of the Zn 2p, Fe 2p, Ag 3d, O 1s, and C 1s energy regions. The high-resolution Zn 2p spectrum in Fig. 3b showed two major fitting peaks centered at 1044.8 and 1021.7 eV, which were assigned to Zn  $2p_{1/2}$  and Zn  $2p_{3/2}$ , respectively, indicating the Zn (II) oxidation state in  $\text{ZnFe}_2\text{O}_4$  [31]. In terms of the Fe 2p spectrum (Fig. 3c), the binding energies for Fe  $2p_{3/2}$  at 713.1 and 711.4 eV correspond to the tetrahedral and octahedral sites, respectively. On the other hand, the peak corresponding to a binding energy of 725.6 eV is in accordance with the Fe  $2p_{1/2}$ , and the two shake-up satellite signals (at 719.3 and 732.8 eV) also suggest that only  $\text{Fe}^{3+}$  exists in  $\text{ZnFe}_2\text{O}_4$  in the nanocomposite sample [32]. These analyses confirmed the Fe (III) oxidation state in the  $\text{ZnFe}_2\text{O}_4$  sample [33,34]. The high-resolution XP spectrum of Ag 3d (Fig. 3d) shows the Ag  $3d_{5/2}$  and Ag

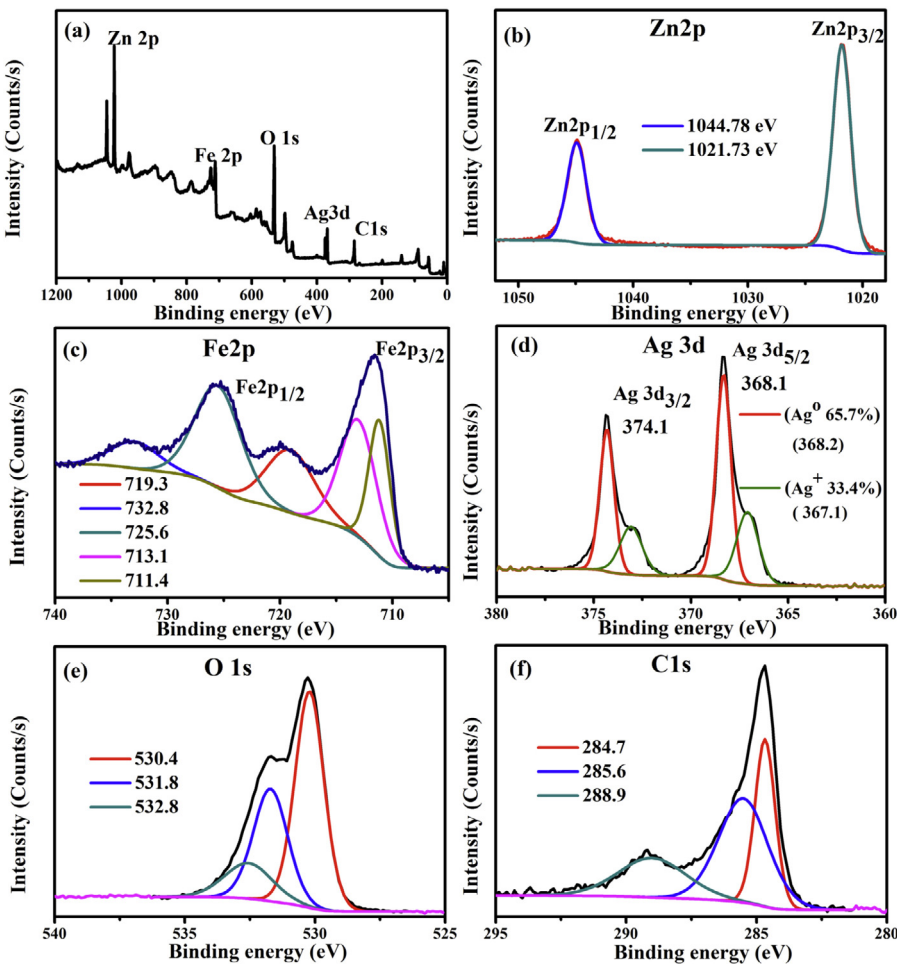


**Fig. 3.** XP spectra of the Ag-ZnFe<sub>2</sub>O<sub>4</sub>@rGO (G80) nanocomposite: (a) survey scan, (b) Zn 2p, (c) Fe 2p, (d) Ag 3d, (e) O 1s, and (f) C 1s energy regions.

3d<sub>3/2</sub> peaks at binding energies of 368.1 and 374.1 eV, respectively. Moreover, the splitting of the 3d doublet of Ag is 6.0 eV, indicating the formation of metallic silver in the Ag-ZnFe<sub>2</sub>O<sub>4</sub>@rGO nanocomposite [35,36]. A detailed deconvolution of the Ag 3d peak was also performed for a better understanding of the chemical state of the silver NPs. The binding energies of Ag 3d<sub>5/2</sub> core level for Ag and AgO were 368.4 and 367.6 eV, respectively. Based on deconvolution analysis, approximately 65.7% of the silver NPs were in the Ag<sup>0</sup> (metallic) state, whereas approximately 33.4% were in the Ag<sup>+</sup> chemical state. The O 1s spectrum (Fig. 3e) can be deconvoluted into three different peaks at 530.4, 531.8, and 532.8 eV. The O 1s binding energy of 530.4 eV was assigned to lattice oxygen binding with Fe and Zn (denoted as Fe–O and Zn–O). In addition, the peaks with binding energies of 531.8 and 532.8 eV were assigned to the surface-absorbed oxygen species, such as O<sub>2</sub><sup>−</sup><sub>ads</sub> and O<sup>−</sup><sub>ads</sub>, and the presence of residual oxygen-containing groups bonded with C atoms in graphene (C–O and C=O), respectively [37–39]. The chemisorbed oxygen on the Ag-ZnFe<sub>2</sub>O<sub>4</sub>@rGO catalyst surface is the most active oxygen, which plays an important role in the oxidation reaction [40].

XPS confirmed the degree of reduction of rGO. Figs. 3f and S3 show typical C 1s XP spectra of the Ag-ZnFe<sub>2</sub>O<sub>4</sub>@rGO nanocomposite and GO, respectively. The peaks for the C 1s signals of the original GO were deconvoluted into several signals, representing C–C and C=C (non-oxygenated) bonds at 284.7 eV, C–O (epoxy and hydroxyl) bond at 285.6 eV, C=O bond at 287.4 eV, and O–C=O (carboxylate) bond at 288.9 eV [41,42]. In Fig. 3f, the peak intensities of C–O and C=O decreased significantly, whereas those of the

C–C and C=C bonds increased remarkably compared to GO. The degree of GO reduction was calculated based on the XPS results. The content of oxygen-containing carbon (including C–O, C=O, and O–C=O) decreased from 87.4% in GO to 69.8% in the nanocomposite, which indicates that GO was reduced to rGO during the reaction under microwave irradiation. The amount of silver in the Ag-ZnFe<sub>2</sub>O<sub>4</sub>@rGO nanocomposite was quantified by ICP-AES and found to be approximately 25% by weight. A possible reason for the high loading is that oxygen-containing groups in the GO sheets act as anchor points for silver nanoparticles, increasing the loading of silver nanoparticles.

Evidence for the reduction of oxygen functional groups on the GO surface was obtained from the FT-IR spectra of GO and Ag-ZnFe<sub>2</sub>O<sub>4</sub>@rGO nanocomposite, as shown in Fig. 4a. In the GO spectrum, the characteristic peaks for the oxygen functional groups on GO were observed, namely the C=O stretching vibrations of COOH groups (1721.04 cm<sup>−1</sup>), O–H deformation vibrations of COOH groups (1625.31 cm<sup>−1</sup>), O–H deformation vibrations of tertiary C–OH (1398.49 cm<sup>−1</sup>), and C–O stretching vibrations of epoxy groups (1056.81 cm<sup>−1</sup>). In addition, the broad absorption peak in the range from 3100 to 3700 cm<sup>−1</sup> was attributed to the O–H stretching vibration. On the other hand, after the microwave-assisted hydrothermal treatment, the peak for C=O disappeared, and the peak intensities of O–H and C–O decreased, indicating the partial reduction of GO, i.e., the removal of oxygen-containing functional groups, leading to the formation of reduced graphene oxide (rGO) in the nanocomposite. Moreover, the two strong absorption peaks in the spectrum of Ag-ZnFe<sub>2</sub>O<sub>4</sub>@rGO at lower frequencies (at

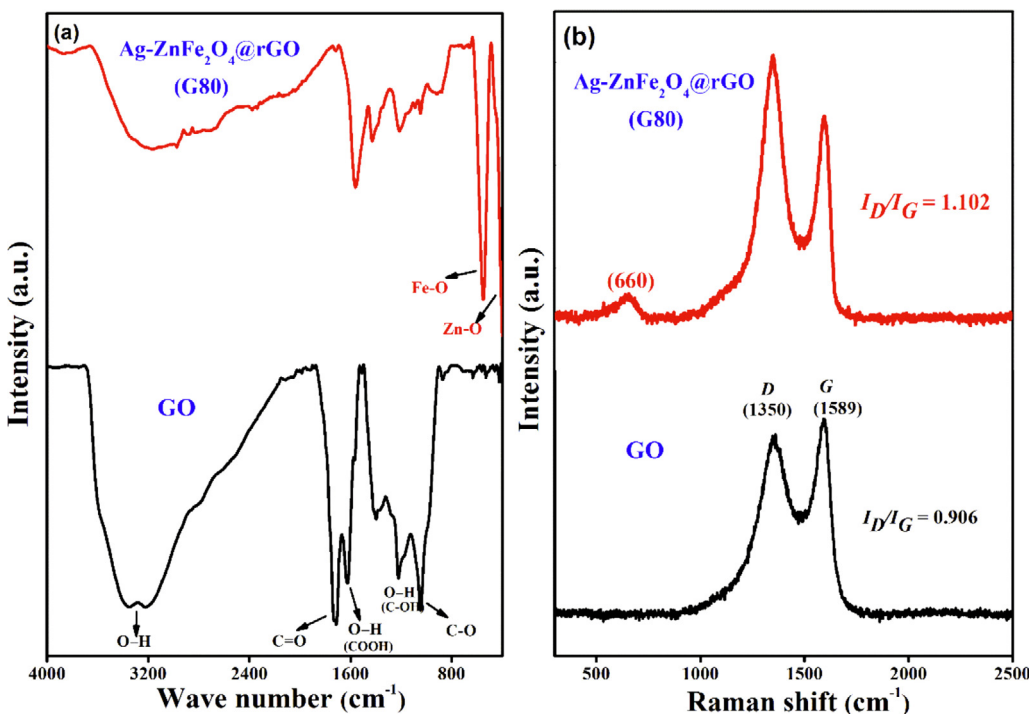


**Fig. 4.** (a) FT-IR spectra of GO and Ag-ZnFe<sub>2</sub>O<sub>4</sub>@rGO (G80) and (b) Raman spectra of GO and Ag-ZnFe<sub>2</sub>O<sub>4</sub>@rGO (G80).

**Table 1**  
Physicochemical properties of the Ag-ZnFe<sub>2</sub>O<sub>4</sub>@rGO (G80) nanocomposite.

$S_{\text{BET}}$ ( $\text{m}^2/\text{g}$ )	Pore Volume ( $\text{cm}^3/\text{g}$ )	Pore Size (nm)
178.77	0.082	3.6

approximately 570.9 and 416.6  $\text{cm}^{-1}$ ) were assigned to the stretching vibrations of Fe—O bonds and Zn—O bonds, respectively. Raman spectra (Fig. 4b) of both GO and Ag-ZnFe<sub>2</sub>O<sub>4</sub>@rGO nanocomposite show two characteristic peaks at about 1350  $\text{cm}^{-1}$  (D-band) originating from the defects and disorder of carbon materials and at 1589  $\text{cm}^{-1}$  (G-band) which is attributed to the vibration of the  $\text{sp}^2$ -bonded carbon atoms. However, the intensity ratio for Ag-ZnFe<sub>2</sub>O<sub>4</sub>@rGO ( $I_D/I_G = 1.102$ ) is larger compared with that of GO ( $I_D/I_G = 0.906$ ), which can be attributed to the decrease in the average size of  $\text{sp}^2$  domains and the increase in the degree of disorder and defects [43,44]. The increase in the  $I_D/I_G$  ratio also confirms that the GO has been deoxygenated and reduced to rGO. For the Ag-ZnFe<sub>2</sub>O<sub>4</sub>@rGO nanocomposite, the Raman spectrum shows one peak at the low frequency region (660  $\text{cm}^{-1}$ ) which is consistent with previous reports on ZnFe<sub>2</sub>O<sub>4</sub>/graphene nanocomposites [23].

### 3.2. BET surface area and pore-size distribution

The N<sub>2</sub> adsorption–desorption isotherm of Ag-ZnFe<sub>2</sub>O<sub>4</sub>@rGO and its corresponding pore-size distribution were investigated, as shown in Fig. 5. According to the IUPAC classification, the Ag-ZnFe<sub>2</sub>O<sub>4</sub>@rGO nanocomposite exhibited the type IV isotherm, indicating its mesoporous nature. The shape of the hysteresis loop is Type H2, indicating the formation of a slit-type pore structure. The Brunauer–Emmett–Teller (BET) specific surface area ( $S_{\text{BET}}$ ) of Ag-ZnFe<sub>2</sub>O<sub>4</sub>@rGO was calculated to be 178.77  $\text{m}^2 \text{ g}^{-1}$ . The inset of Fig. 5 presents the corresponding Barrett–Joyner–Halenda (BJH) pore-size distribution (PSD) of the Ag-ZnFe<sub>2</sub>O<sub>4</sub>@rGO product, showing a sharp maximum at approximately 3.6 nm (Table 1), confirming the mesoporous nature of the nanocomposite. During the photocatalytic reaction, more adsorption/reaction sites can be pro-

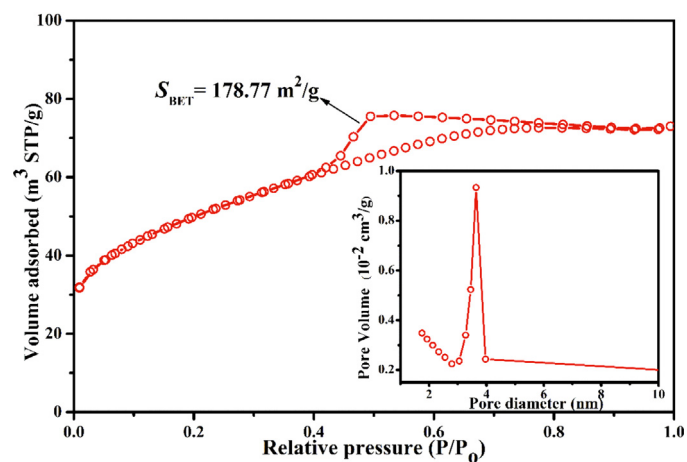


**Fig. 5.** N<sub>2</sub> adsorption–desorption isotherm of Ag-ZnFe<sub>2</sub>O<sub>4</sub>@rGO (G80). The inset presents the corresponding pore-size distribution.

vided through the larger surface area, which can contribute to the improvement in photocatalytic activity.

Fig. 6 shows two distinct weight losses from the TGA profile in air with a total weight loss of 19% in the two temperature ranges of 20–120 °C and 250–400 °C, representing the loss of adsorbed water (3.8 wt%) and the burn-out of graphene (15.2 wt%), respectively. Based on this, the rGO content was estimated to be approximately 15.2 wt% of the nanocomposite. In addition, a strong exothermic peak at 320 °C was observed in the DSC curve, which was assigned to combustion and decomposition of the carbon skeleton. Under nitrogen flow, the Ag-ZnFe<sub>2</sub>O<sub>4</sub>@rGO nanocomposite showed high thermal stability with no sudden weight loss up to 800 °C. This is consistent with the thermal behavior of graphene itself under a nitrogen atmosphere, as reported elsewhere [45].

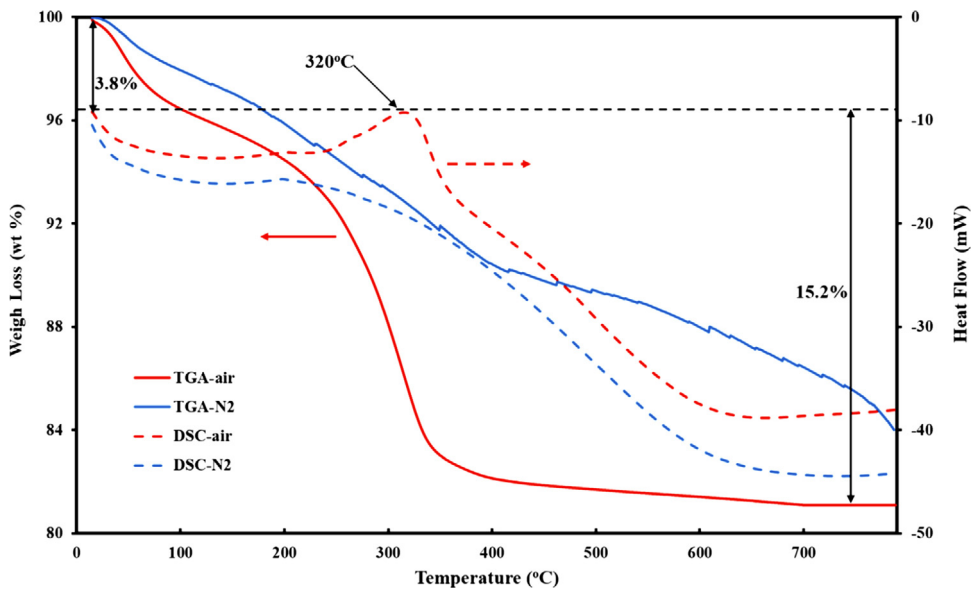


**Fig. 6.** TGA and DSC curves of Ag-ZnFe<sub>2</sub>O<sub>4</sub>@rGO (G80) nanocomposite in air and nitrogen atmospheres.

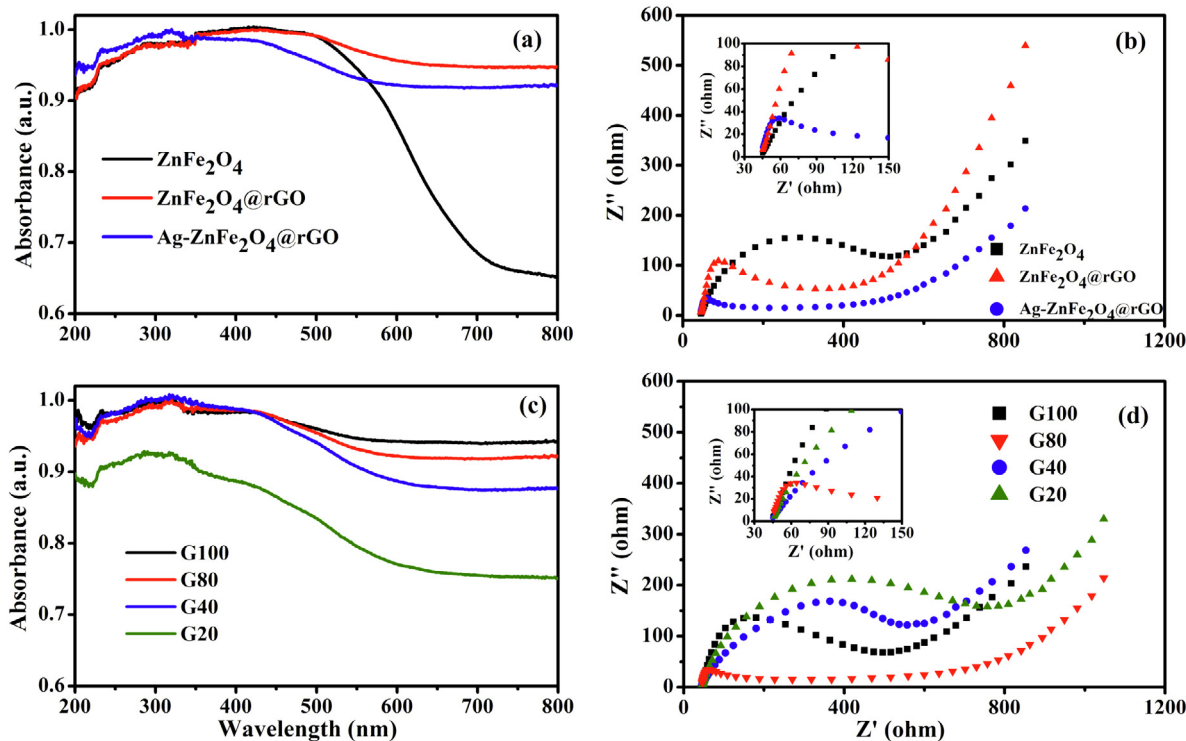


**Fig. 7.** UV-vis absorption spectra (a) and EIS spectra (b) of bare ZnFe<sub>2</sub>O<sub>4</sub>, ZnFe<sub>2</sub>O<sub>4</sub>@rGO, and Ag-ZnFe<sub>2</sub>O<sub>4</sub>@rGO (G80); UV-vis absorption spectra (c) and EIS spectra (d) of Ag-ZnFe<sub>2</sub>O<sub>4</sub>@rGO prepared using different GO concentrations (G20, G40, G80, and G100).

### 3.3. UV-vis spectroscopy

**Fig. 7a** shows the UV-vis absorption spectra of ZnFe<sub>2</sub>O<sub>4</sub>, ZnFe<sub>2</sub>O<sub>4</sub>@rGO, and Ag-ZnFe<sub>2</sub>O<sub>4</sub>@rGO nanocomposites. The bare ZnFe<sub>2</sub>O<sub>4</sub> showed wide absorption in the visible region with an absorption edge at approximately 700 nm, corresponding to a band gap of approximately 1.9 eV. The introduction of rGO increased the absorbance intensity of the composites substantially. The enhancement of visible-light absorption for the nanocomposites is caused mainly by the background absorption of rGO, as well as by the SPR effect of Ag NPs [46]. On the other hand, there is almost no change

in the location of the end of the absorption band with increasing rGO content, which means that the introduction of rGO has little effect on the band gap of ZnFe<sub>2</sub>O<sub>4</sub> (**Fig. 7c**).

### 3.4. Electrochemical impedance spectra (EIS) and photocurrent response

One of the important roles of graphene is its ability to act as an electron acceptor and transfer channel to facilitate the separation and migration of photogenerated electrons. As shown in **Fig. 7b**, the semicircle in the EIS plot became smaller with the introduc-

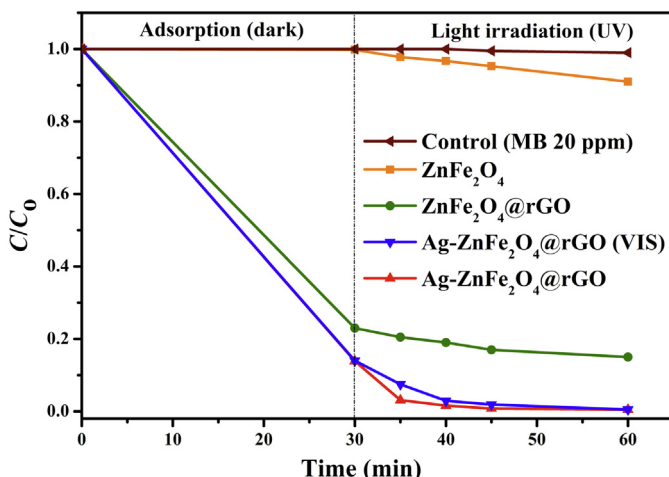


**Fig. 8.** Degradation of MB (at 20 ppm) on  $\text{ZnFe}_2\text{O}_4$ ,  $\text{ZnFe}_2\text{O}_4@\text{rGO}$ , and  $\text{Ag-ZnFe}_2\text{O}_4@\text{rGO}$  (G80) under UV light ( $\lambda = 365 \text{ nm}$ ).  $\text{Ag-ZnFe}_2\text{O}_4@\text{rGO}$  (G80) was also tested under visible light ( $\lambda > 420 \text{ nm}$ ) for comparison.

tion of reduced graphene oxide and Ag NPs, indicating a decrease in the solid-state interface-layer resistance and the charge-transfer resistance on the surface. Overall, both the electron-accepting and transport properties of graphene in the nanocomposite can contribute to the suppression of charge recombination; thus, a higher rate of photocatalysis would be achieved. The EIS Nyquist plots (Fig. 8d) of G80 and G100 exhibit much smaller semicircles, indicating a significant decrease in the charge-transfer resistance in the  $\text{Ag-ZnFe}_2\text{O}_4@\text{rGO}$  nanocomposites. Notably, G80 shows the smallest semicircle, suggesting that there is an optimal GO content for the best charge-transfer capability. The higher charge-transfer resistance in G100 was attributed to the excessive addition of rGO, which may act as a new recombination center for photogenerated electrons and holes that hinders the migration of photogenerated electrons from the interior to the surface of the nanocomposite. In addition, the excessive loading of black-colored rGO shields the active sites on the catalyst surface and decreases the intensity of light passing through the reaction solution.

Photocurrent measurements were carried out for pure  $\text{ZnFe}_2\text{O}_4$  and  $\text{Ag-ZnFe}_2\text{O}_4@\text{rGO}$  after deposition on the FTO electrodes via several on-off cycles of irradiation. The photocurrent transient responses under UV-light irradiation and in the dark for these samples were measured at a potential of 0 V vs. SCE in a 0.5 M  $\text{Na}_2\text{SO}_4$  aqueous solution (Fig. S4). The photocurrent of the  $\text{Ag-ZnFe}_2\text{O}_4@\text{rGO}$  electrode (190 nA) was approximately 8 times higher than that of the pure  $\text{ZnFe}_2\text{O}_4$  electrode (24 nA), indicating significantly enhanced separation efficiency of the photoinduced electrons and holes as a result of the electronic interactions between the Ag and  $\text{ZnFe}_2\text{O}_4$  nanoparticles and graphene sheets.

### 3.5. Photocatalytic activity and stability

In the present study, the photocatalytic removal of MB under UV- and visible-light irradiation using the  $\text{Ag-ZnFe}_2\text{O}_4@\text{rGO}$  nanocomposite as a catalyst was investigated. MB is a model pollutant for photocatalytic degradation and a representative organic dye in textile effluents. From Figs. 8 and 9, MB showed only approximately 9% degradation after 30 min under UV irradiation using bare  $\text{ZnFe}_2\text{O}_4$ . On the other hand, the photocatalytic activity of  $\text{ZnFe}_2\text{O}_4$  was enhanced significantly to 85% after 30 min by the introduction of rGO. Similarly, by introducing the Ag NPs to the composite, the rate of degradation was enhanced to 99.8% due to the SPR effect of Ag NPs under both UV- and visible-light irradiation [47]. The specific catalytic properties of the Ag NPs are related directly to their

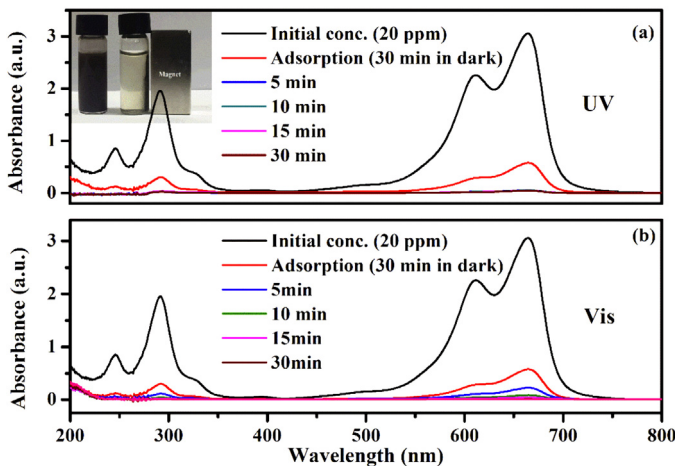
sizes and the degree of dispersion on the graphene sheet. The effects of the Ag dosage was studied (Fig. S5). The photocatalytic activity increased with increasing amount of 0.1 M  $\text{AgNO}_3$  up to 10 ml, but then decreased with further increases in the amount of  $\text{AgNO}_3$  solution added, which may be due to the aggregation of Ag NPs into large particles. The  $\text{Ag-ZnFe}_2\text{O}_4@\text{rGO}$  nanocomposites exhibited increasing adsorption properties with increasing rGO content (Fig. 10a). During adsorption, the dye molecules were transferred from the bulk solution to the nanocomposite surface and were adsorbed with an offset face-to-face orientation via  $\pi-\pi$  conjugation between MB and the aromatic regions of the graphene sheets [48–50]. Fig. 10b shows the concentration changes of MB during the photodegradation process under UV irradiation. During irradiation, the photo-excited electrons can be injected quickly between the graphene layers and then react with  $\text{O}_2$  molecules adsorbed on the surface of the graphene layers to generate  $\cdot\text{O}_2^-$  radicals [51,52]. In this way, the prepared nanocomposite could generate more electrons and holes as well as more superoxide anions [51]. As a result of the production of  $\cdot\text{O}_2^-$  radicals, dyes can be oxidized to  $\text{H}_2\text{O}$ ,  $\text{CO}_2$ , and other mineralization products. Charge recombination is suppressed in the  $\text{Ag-ZnFe}_2\text{O}_4@\text{rGO}$  nanocomposite due to the electron-transfer process, and the efficiency of the photocatalytic properties is largely enhanced. Applying the parameters used in the present study, when the rGO content was approximately 15.2 wt% (G80), the photocatalytic performance was at a maximum and was measured to be approximately 99.8% under 30 min of UV irradiation.

Fig. 11(a and b) shows the universality of the obtained nanocomposite for the photodecomposition of different types of dyes (here, MB, RhB, and MO). The plots concentration versus time show that using  $\text{Ag-ZnFe}_2\text{O}_4@\text{rGO}$  photocatalysts under UV light yields faster dye removal compared to that of using the composites under visible light. MB could be degraded completely within 15 and 30 min under UV and visible light, respectively. Approximately 95.5% and 77% of RhB and MO could be degraded, respectively, after 30 min of UV irradiation. In addition, approximately 95% and 72% of RhB and MO, respectively, could be degraded within 30 min of visible-light irradiation. The nanocomposite showed better photocatalytic degradation performance for cationic dyes (MB and RhB) than for an anionic dye (MO). This is because the cationic dyes are much easier to adsorb on the negatively charged nanocomposite than anionic dyes. Furthermore, the photocatalytic degradation activity of RhB is less than that of MB, which is due to the larger and more complex structure of the RhB molecules.

The photocatalytic degradation kinetics of MB follows pseudo-first-order behavior. The rate constants ( $k$ ) of the photocatalytic degradation of MB, RhB, and MO under both UV- and visible-light irradiation at 25 °C were calculated using Eq. (1). Fig. 12 and Fig. S6(a and b) show the pseudo-first-order rate constant for the photodecomposition of 10 ppm of MB, RhB, and MO using  $\text{Ag-ZnFe}_2\text{O}_4@\text{rGO}$  photocatalysts under both UV and visible light. Among the calculated values, the rate constant of MB degradation under UV irradiation was the highest ( $k = 0.415 \text{ min}^{-1}$ ), 2.3 times higher than that for the visible-light process.

### 3.6. Reusability test

In addition to the photocatalytic activity, stability is another important factor for determining the use of the catalysts in practical applications. The photocatalytic stability of the  $\text{Ag-ZnFe}_2\text{O}_4@\text{rGO}$  nanocomposite was examined by repeated photocatalytic experiments using the magnetic property of the nanocomposite. As shown in Fig. 13,  $\text{Ag-ZnFe}_2\text{O}_4@\text{rGO}$  exhibited no obvious decrease in the photocatalytic degradation efficiency after five cycles. This indicates the possibility of using the catalyst for a longer operation time. The structure of the nanocomposite remained relatively



**Fig. 9.** Comparison of the photocatalytic degradation of MB using Ag-ZnFe<sub>2</sub>O<sub>4</sub>@rGO (G80) under UV light (a) and visible light (b). (Inset: The G80 nanocomposite photocatalyst was easily separated using a magnet).

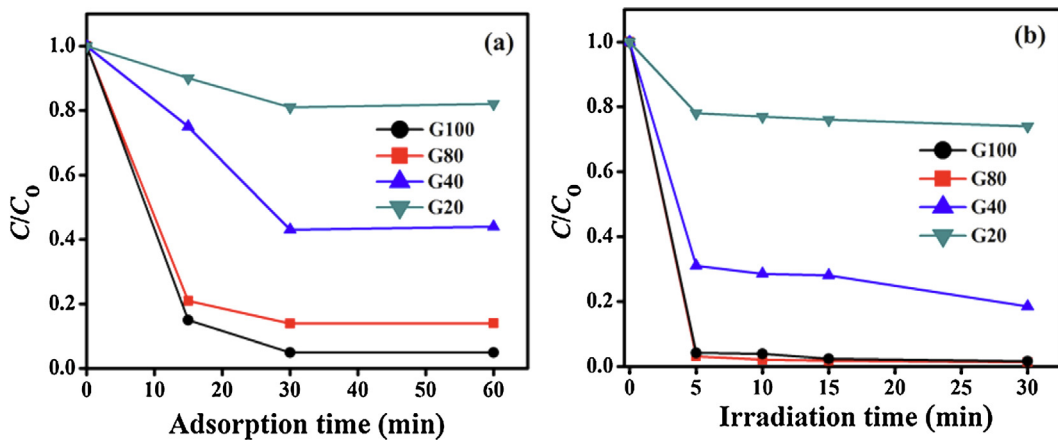


**Fig. 10.** Variation in the adsorption (a) and photocatalytic degradation (b) of MB for Ag-ZnFe<sub>2</sub>O<sub>4</sub>@rGO photocatalysts prepared with different amounts of GO.

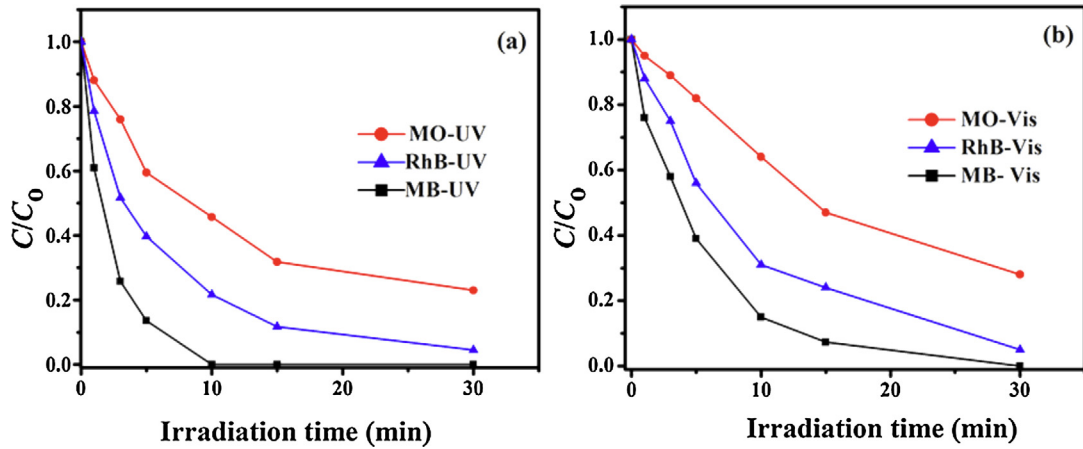


**Fig. 11.** Degradation of 10 ppm of three different dyes (MO, RhB, and MB) in aqueous solution using the Ag-ZnFe<sub>2</sub>O<sub>4</sub>@rGO (G80) nanocomposite photocatalyst under UV- (a) and visible-light (b) irradiation.

stable as shown in the FE-SEM and TEM images of the used catalyst in Fig. S7. The FT-IR spectra of the used catalyst showed similar characteristic absorption bands to the fresh catalyst, as shown in Fig. S8. The only difference was observed in the range of 1000–1300 cm<sup>-1</sup>, which revealed the deposition of some organic materials on the surface of the used catalyst. Likewise, the diffraction pattern of the used nanocomposite after 5 cycles showed no

noticeable deviation from that of the fresh nanocomposite (Fig. S9). These findings indicate excellent long-term stability and reusability of the Ag-ZnFe<sub>2</sub>O<sub>4</sub>@rGO nanocomposite for the degradation of organic pollutants in water compared with the other prepared materials mentioned in literature (Fig. S10) [7,22].

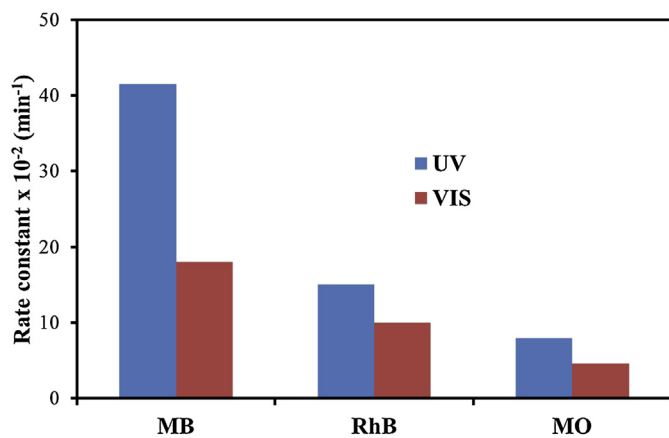


**Fig. 12.** Pseudo-first-order rate constants ( $k$ ) for the photodegradation of MB, RhB, and MO (all in an aqueous solution of 10 ppm) by the Ag-ZnFe<sub>2</sub>O<sub>4</sub>@rGO (G80) photocatalyst under UV- and visible-light irradiation.

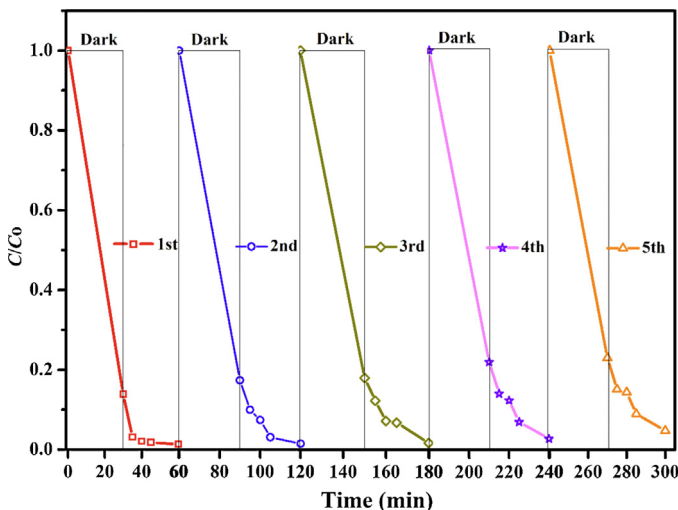


**Fig. 13.** Reusability test of the Ag-ZnFe<sub>2</sub>O<sub>4</sub>@rGO (G80) catalyst for the photodegradation of MB (20 ppm) using 0.5 g cat l<sup>-1</sup> and UV lamp ( $\lambda = 365$  nm) at 40 W.

### 3.7. Photocatalytic reaction mechanism

To understand the photocatalytic mechanism, the main active oxidant in the photocatalytic reaction process should be identified. The oxidants generated in the photocatalytic process can be measured through the addition of trapping or scavenging reagents. Isopropyl alcohol (IPA), NaHCO<sub>3</sub>, and *p*-benzoquinone (BZQ) are used as scavengers for the hydroxyl radical ( $\cdot\text{OH}$ ), the hole ( $\text{h}_{\text{VB}}^+$ ), and the superoxide radical ( $\cdot\text{O}_2^-$ ), respectively. The results in Fig. 14 show that the degradation of MB was decelerated after the addition of NaHCO<sub>3</sub> (0.1 M) or BZQ (0.001 M) in the current photocatalytic system, implying that the holes ( $\text{h}_{\text{VB}}^+$ ) and superoxide radicals ( $\cdot\text{O}_2^-$ ) are the major active species responsible for the oxidation of MB under UV irradiation. Moreover, the addition of IPA (0.1 M) has a negligible effect on MB degradation. This shows that the hydroxyl radicals ( $\cdot\text{OH}$ ) make a very small contribution to the photocatalytic reaction.

Based on these results, a mechanism for the increased photocatalytic activity over the as-prepared Ag-ZnFe<sub>2</sub>O<sub>4</sub>@rGO nanocomposite is proposed as follows (see also Fig. 15):

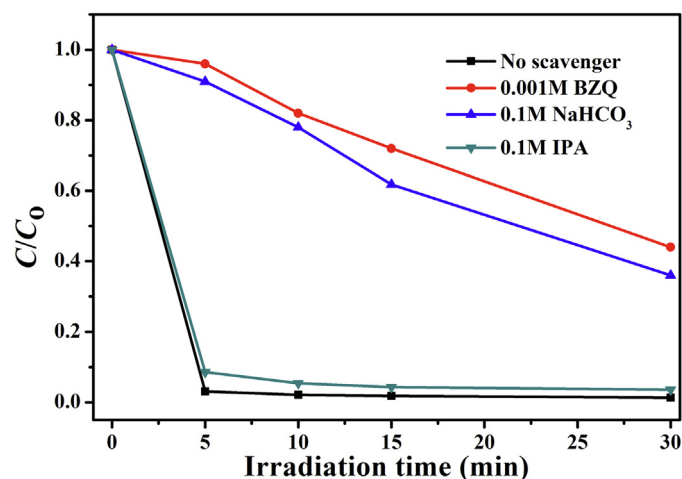
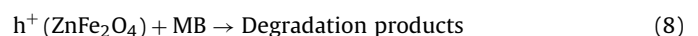
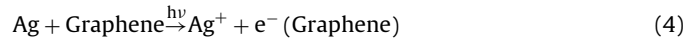


**Fig. 14.** Trapping of superoxide radicals, holes, and hydroxide radicals (reactive species) by BZQ, NaHCO<sub>3</sub>, and IPA, respectively, during the photodegradation reaction on the Ag-ZnFe<sub>2</sub>O<sub>4</sub>@rGO (G80) nanocomposite catalyst.



When the nanocomposite was irradiated with UV or visible light in the presence of an aqueous solution of an organic compound (e.g., MB dye), ZnFe<sub>2</sub>O<sub>4</sub> is excited by photons, and electron-hole pairs are generated (Eq. (2)). The photogenerated electrons can transfer readily from the conduction band of ZnFe<sub>2</sub>O<sub>4</sub> to the surface of the graphene nanosheets because the conduction band of graphene (-0.75 V vs. normal hydrogen electrode (NHE)) [3] is more positive than that of ZnFe<sub>2</sub>O<sub>4</sub> (-1.54 V vs. NHE) [53] (Eq. (3)). At the same time, Ag NPs can absorb light and generate electrons due to the SPR effect [46], plasmon-induced electrons on the Ag NPs can flow to the conduction band (CB) of graphene rather than ZnFe<sub>2</sub>O<sub>4</sub>, owing to the less negative CB bottom of graphene compared to that of ZnFe<sub>2</sub>O<sub>4</sub> (Eq. (4)), and Ag NPs can also accept electrons from the conduction band of ZnFe<sub>2</sub>O<sub>4</sub> for enhancing the charge separation [25]. A portion of the CB electrons on ZnFe<sub>2</sub>O<sub>4</sub> tends to shift to the positive-potential Ag<sup>+</sup> NPs and changes some Ag<sup>+</sup> NPs to Ag NPs (Eq. (5)), whereas the other electrons can be scavenged by O<sub>2</sub> in the water, resulting in superoxide anion free radicals ( $\cdot\text{O}_2^-$ ) (Eq. (6)), which are the main active species in the reaction with organic dyes (Eq. (7)). Moreover, the reactive holes at the valence band (VB) of ZnFe<sub>2</sub>O<sub>4</sub> will oxidize MB directly, because the potential of the VB of ZnFe<sub>2</sub>O<sub>4</sub> (0.38 V vs. NHE) [53] is more negative than the potential required to oxidize the adsorbed H<sub>2</sub>O on the surface to  $\cdot\text{OH}$ . ( $E_{\cdot\text{OH}/\text{H}_2\text{O}} = 2.87$  V vs. NHE) [54] (Eq. (8)). As a result, the separation efficiency of the photogenerated charge carriers is effectively improved at the interface of the nanocomposite, which allows more participation of holes in the photocatalytic reaction.

### 4. Conclusions

This paper reports the preparation of a magnetically separable Ag-ZnFe<sub>2</sub>O<sub>4</sub>@rGO nanocomposite with various content of reduced graphene oxide. The nanocomposites were synthesized using a simple one-pot microwave-assisted hydrothermal method, where the reduction of GO to rGO was achieved with the simultaneous in-situ deposition of ZnFe<sub>2</sub>O<sub>4</sub> NPs and Ag NPs on the rGO nanosheets.

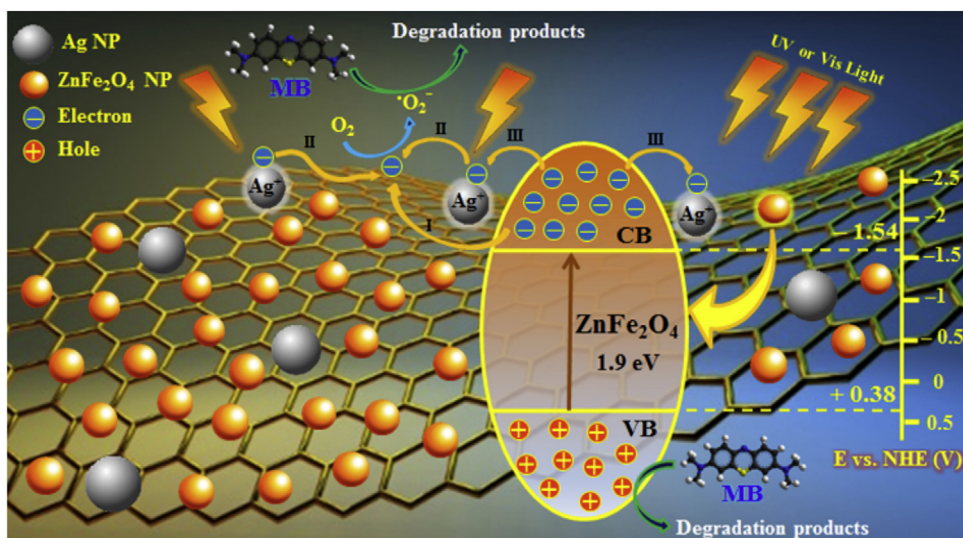


**Fig. 15.** Schematic diagram of the MB degradation mechanism on Ag-ZnFe<sub>2</sub>O<sub>4</sub>@rGO (G80) under UV- or visible-light irradiation. Conduction band potential of rGO,  $E_{rGO} = -0.75$  V vs. NHE; potential required to convert H<sub>2</sub>O to •OH,  $E_{OH/H_2O} = 2.87$  V vs. NHE.

The Ag-ZnFe<sub>2</sub>O<sub>4</sub>@rGO nanocomposites exhibit high photocatalytic performance for MB, RhB, and MO degradation under both UV- and visible-light irradiation. This excellent photocatalytic activity was attributed to the extended light-response range of the nanocomposite due to the synergistic interaction among the Ag NPs, ZnFe<sub>2</sub>O<sub>4</sub> NPs, and graphene nanosheets. Both the Ag NPs and graphene nanosheets can facilitate the efficient separation, acceptance, and transportation of the ZnFe<sub>2</sub>O<sub>4</sub> conduction band electrons ( $e^{-}_{CB}$ ), and the mutual strong interfacial contact between Ag or ZnFe<sub>2</sub>O<sub>4</sub> and graphene can accelerate the direct transport of  $e^{-}_{CB}$  to the graphene sheets, which can in turn extend the lifetime of the charge carriers and enhance the quantum efficiency of ZnFe<sub>2</sub>O<sub>4</sub>. Furthermore, the effective separation of  $e^{-}_{CB}$  and  $h^{+}_{VB}$  can provide  $e^{-}_{CB}$  with sufficient time to participate in the multiple-electron reduction reaction of oxygen, leading to the generation of superoxide anion free radicals ( $\bullet O_2^-$ ), which were identified as the dominant active species in the photodegradation process. The Ag-ZnFe<sub>2</sub>O<sub>4</sub>@rGO nanocomposite could be reused five times without significant loss of the photocatalytic activity, therefore, acting as an efficient photocatalyst to decompose organic pollutants in aqueous solutions.

## Acknowledgments

This study was supported by the 2015 Postdoctoral Fellowship Program for Foreign Researchers (NRF-2015K2A4A1036188) and the Priority Research Centers Program (2014R1A6A1031189), both of the National Research Foundation, the Republic of Korea.

## Appendix A. Supplementary data

Supplementary data associated with this article can be found, in the online version, at <http://dx.doi.org/10.1016/j.apcatb.2016.10.033>.

## References

- [1] K. Ji, J. Deng, H. Zang, J. Han, H. Arandiyan, H. Dai, *Appl. Catal. B: Environ.* 165 (2015) 285–295.
- [2] C. Hachem, F. Bocquillon, O. Zahraa, M. Bouchy, *Dyes Pigm.* 49 (2001) 117–125.
- [3] D. Xu, B. Cheng, S. Cao, J. Yu, *Appl. Catal. B* 164 (2015) 380–388.
- [4] F.Z. Yehia, N.G. Kandile, A.M. Badawi, A.H. Mady, *Clean Soil Air Water* 40 (2012) 692–697.
- [5] J. Ding, W. Yan, S. Sun, J. Bao, C. Gao, *ACS Appl. Mater. Interfaces* 6 (2014) 12877–12884.
- [6] A. Di Paola, E. García-López, G. Marcà, L. Palmisano, *J. Hazard. Mater.* 211–212 (2012) 3–29.
- [7] F.A. Jumeri, H.N. Lim, S.N. Ariffin, N.M. Huang, P.S. Teo, S.O. Fatin, C.H. Chia, I. Harrison, *Ceram. Int.* 40 (2014) 7057–7065.
- [8] V.H. Nguyen, J.-J. Shim, *Mater. Sci. Eng. B* 180 (2014) 38–45.
- [9] S. Wang, Z. Ding, X. Wang, *Chem. Commun.* 51 (2015) 1517–1519.
- [10] S. Wang, Y. Hou, X. Wang, *ACS Appl. Mater. Interfaces* 7 (2015) 4327–4335.
- [11] M. Jiang, Y. Gao, Z. Wang, Z. Ding, *Appl. Catal. B: Environ.* 198 (2016) 180–188.
- [12] Z. Wang, M. Jiang, J. Qin, H. Zhou, Z. Ding, *Phys. Chem. Chem. Phys.* 17 (2015) 16040–16046.
- [13] L. Tang, V.H. Nguyen, J.-J. Shim, *Mater. Res. Bull.* 71 (2015) 53–60.
- [14] S. Wu, P. Wang, Y. Cai, D. Liang, Y. Ye, Z. Tian, J. Liu, C. Liang, *RSC Adv.* 5 (2015) 9069–9074.
- [15] C. Cai, Z. Zhang, J. Liu, N. Shan, H. Zhang, D.D. Dionysiou, *Appl. Catal. B: Environ.* 182 (2016) 456–468.
- [16] J. Xie, Q. Wu, D. Zhao, *Carbon* 50 (2012) 800–807.
- [17] J. Qu, L. Shi, C. He, F. Gao, B. Li, Q. Zhou, H. Hu, G. Shao, X. Wang, J. Qiu, *Carbon* 66 (2014) 485–492.
- [18] M.R. Hoffmann, S.T. Martin, W. Choi, D.W. Bahnemann, *Chem. Rev.* 95 (1995) 69–96.
- [19] Y. Fu, H. Chen, X. Sun, X. Wang, *Appl. Catal. B: Environ.* 111–112 (2012) 280–287.
- [20] S. Bai, X. Shen, X. Zhong, Y. Liu, G. Zhu, X. Xu, K. Chen, *Carbon* 50 (2012) 2337–2346.
- [21] H.H. El-Maghrabi, E.A. Nada, F.S. Soliman, Y.M. Moustafa, A. El-Sayed Amin, *Egypt. J. Petrol.* (2016), <http://dx.doi.org/10.1016/j.ejpe.2015.12.004>.
- [22] Y. Yao, J. Qin, Y. Cai, F. Wei, F. Lu, S. Wang, *Environ. Sci. Pollut. Res.* 21 (2014) 7296–7306.
- [23] Y. Fu, X. Wang, *Ind. Eng. Chem. Res.* 50 (2011) 7210–7218.
- [24] Z. Zhu, F. Liu, H. Zhang, J. Zhang, L. Han, *RSC Adv.* 5 (2015) 55499–55512.
- [25] N. Khadgi, Y. Li, A.R. Upreti, C. Zhang, W. Zhang, Y. Wang, D. Wang, *Photochem. Photobiol.* 92 (2016) 238–246.
- [26] X. Fan, J. Shao, Z. Li, F. Ma, A. Meng, Q. Li, *New J. Chem.* 40 (2016) 1330–1335.
- [27] Y. Haldorai, J.-J. Shim, *Compos. Interface* 20 (2013) 365–377.
- [28] P. Tang, G. Hu, Y. Gao, W. Li, S. Yao, Z. Liu, D. Ma, *Sci. Rep.* 4 (2014) 5901, <http://dx.doi.org/10.1038/srep05901>.
- [29] D.C. Marcano, D.V. Kosynkin, J.M. Berlin, A. Sinitskii, Z. Sun, A. Slesarev, L.B. Alemany, W. Lu, J.M. Tour, *ACS Nano* 4 (2010) 4806–4816.
- [30] M. Ge, N. Zhu, Y.P. Zhao, J. Li, L. Liu, *Ind. Eng. Chem. Res.* 51 (2012) 5167–5173.
- [31] L. Sun, R. Shao, L. Tang, Z. Chen, *J. Alloys Compd.* 564 (2013) 55–62.
- [32] X. Zhou, B. Wang, H. Sun, C. Wang, P. Sun, X. Li, X. Hua, G. Lu, *Nanoscale* 8 (2016) 5446–5453.
- [33] L.R. Hou, L. Lian, L.H. Zhang, G. Pang, C.Z. Yuan, X.G. Zhang, *Adv. Funct. Mater.* 25 (2015) 238–246.
- [34] H.J. Lv, L. Ma, P. Zeng, D.N. Ke, T.Y. Peng, *J. Mater. Chem.* 20 (2010) 3665–3672.
- [35] J. Cao, B. Luo, H. Lin, S. Chen, *J. Mol. Catal. A: Chem.* 344 (2011) 138–144.
- [36] J. Cao, B. Luo, H. Lin, B. Xu, S. Chen, *J. Hazard. Mater.* 217–218 (2012) 107–115.
- [37] D. Andreeva, T. Tabakova, V. Idakiev, P. Christov, R. Giovanoli, *Appl. Catal. A: General* 169 (1998) 9–14.
- [38] S. Wang, J. Zhang, J. Yang, X. Gao, H. Zhang, Y. Wang, Z. Zhu, *RSC Adv.* 5 (2015) 10048–10057.

- [39] H.C. Schniepp, J.-L. Li, M.J. McAllister, H. Sai, M. Herrera-Alonso, D.H. Adamson, R.K. Prud'homme, R. Car, D.A. Saville, I.A. Aksay, *J. Phys. Chem. B* 110 (2006) 8535–8539.
- [40] L. Xu, J. Wang, *Environ. Sci. Technol.* 46 (2012) 10145–10153.
- [41] Y. Haldorai, A. Rengaraj, C.H. Kwak, Y.S. Huh, Y.-K. Han, *Synth. Met.* 198 (2014) 10–18.
- [42] T. Jiao, H. Guo, Q. Zhang, Q. Peng, Y. Tang, X. Yan, B. Li, *Sci. Rep.* 5 (2015), <http://dx.doi.org/10.1038/srep11873>.
- [43] S.V. Kumar, N.M. Huang, N. Yusoff, H.N. Lim, *Mater. Lett.* 93 (2013) 411–414.
- [44] T.N. Narayanan, Z. Liu, P.R. Lakshmy, W. Gao, Y. Nagaoka, D.S. Kumar, J. Lou, R. Vajtai, P.M. Ajayan, *Carbon* 50 (2012) 1338–1345.
- [45] Z. Ji, X. Shen, Y. Song, G. Zhu, *Mater. Sci. Eng. B* 176 (2011) 711–715.
- [46] J. Yin, C. Yue, Y. Zang, C.-H. Chiu, J. Li, H.-C. Kuo, Z. Wu, J. Li, Y. Fang, C. Chen, *Nanoscale* 5 (2013) 4436–4442.
- [47] K.C. Hsu, D.H. Chen, *Nanoscale Res. Lett.* 9 (2014) 193.
- [48] H. Zhang, X.J. Lv, Y.M. Li, Y. Wang, J.H. Li, *ACS Nano* 4 (2010) 380–386.
- [49] Q.J. Xiang, J.G. Yu, M. Jaromiec, *Chem. Soc. Rev.* 41 (2012) 782–796.
- [50] S.D. Perera, R.G. Mariano, K. Vu, N. Nour, O. Seitz, Y. Chabal, K.J. Balkus Jr., *ACS Catal.* 2 (2012) 949–956.
- [51] D.-H. Yoo, T.V. Cuong, V.H. Pham, J.S. Chung, N.T. Khoa, E.J. Kim, S.H. Hahn, *Curr. Appl. Phys.* 11 (2011) 805–808.
- [52] Y.L. Min, K. Zhang, Y.C. Chen, Y.G. Zhang, *Sep. Purif. Technol.* 86 (2012) 98–105.
- [53] X. Li, D. Tang, F. Tang, Y. Zhu, C. He, M. Liu, C. Lin, Y. Liu, *Mater. Res. Bull.* 56 (2014) 125–133.
- [54] T. Ichino, R.W. Fessenden, *J. Phys. Chem. A* 111 (2007) 2527–2541.